

# Level Set based Reconstruction Algorithm for EIT Lung Images: First Clinical Results

Peyman Rahmati<sup>1</sup>, Manuchehr Soleimani<sup>2</sup>, Sven Pulletz<sup>3</sup>, Inéz Frerichs<sup>3</sup>, and Andy Adler<sup>1</sup>

<sup>1</sup> Department of Systems and Computer Eng., Carleton University, ON., Canada

<sup>2</sup> Department of Electronic & Electrical Engineering, University of Bath, UK

<sup>3</sup> Department of Anaesthesiology and Intensive Care Medicine, University Medical Centre Schleswig-Holstein, Campus Kiel, Kiel, Germany

E-mail: [prahmati@sce.carleton.ca](mailto:prahmati@sce.carleton.ca), [m.soleimani@bath.ac.uk](mailto:m.soleimani@bath.ac.uk),  
[pulletz@anaesthesie.uni-kiel.de](mailto:pulletz@anaesthesie.uni-kiel.de), [frerichs@anaesthesie.uni-kiel.de](mailto:frerichs@anaesthesie.uni-kiel.de),  
[adler@sce.carleton.ca](mailto:adler@sce.carleton.ca)

**Abstract.** We show the first clinical results using the level set based reconstruction algorithm for electrical impedance tomography data. The level set based reconstruction method allows reconstruction of non-smooth interfaces between image regions, which are typically smoothed by traditional voxel based reconstruction methods. We develop a time difference formulation of the level set based reconstruction method for 2D images. The proposed reconstruction method is applied to reconstruct clinical electrical impedance tomography data of a slow flow inflation pressure-volume manoeuvre in lung healthy and adult lung injury patients. Images from the level set based reconstruction method and the voxel based reconstruction method are compared. The results show comparable reconstructed images, but with an improved ability to reconstruct sharp conductivity changes in the distribution of lung ventilation using the level set based reconstruction method.

## 1. Introduction

Tomographic imaging systems seek to see the inside objects, by introducing energy and measuring its interaction with the medium. Electrical Impedance Tomography (EIT) measures the internal impedance distribution using surface measurements. Electrical current is applied to the medium and the voltage at the surface is measured using electrodes. The impedance distribution is then estimated based on the measured voltages and medium geometry. Some of typical applications of these techniques are for geophysical imaging (Loke and Barker 1996a 1996b; Church 2006), process monitoring (Soleimani *et al* 2006a; Manwaring *et al* 2008), and functional imaging of the body (Frerichs 2000; Frerichs *et al* 2001; Gao *et al* 2006; Adler *et al* 2009; Frerichs *et al* 2010; Rahmati *et al* 2011; Pulletz *et al* 2011).

In this paper, we focus on image reconstruction in EIT using the level set (LS) approach. The LS approach has become popular because of its ability to track

propagating interfaces (Osher and Sethian 1988; Sethian 1999), and more recently it has been applied in variety of applications in inverse problems and in image processing (Santosa *et al* 1996; Litman *et al* 1998; Dorn *et al* 2000; Osher and Paragios 2003). Level set based reconstruction method (LSRM) is a nonlinear inversion scheme using Gauss-Newton (GN) optimization approach to iteratively reduce a given cost functional, which is the norm of the difference between the simulated and measured data. In comparison to the voxel based reconstruction method (VBRM) ( e.g. Polydorides *et al* 2002), the LSRM has the advantage of introducing the conductivity of background and that of inclusions as known priori information into the reconstruction algorithm, enabling it to reconstruct sharp contrasts (Soleimani *et al* 2006a). The unknown parameters to be recovered from the data are the size, number, shapes of the inclusions. These unknown parameters are given as the zero LS of a higher dimensional function, called level set function (LSF). In every iteration, the LSF is modified according to an update formula to modify the shape of the inclusion at its zero LS (see figure 1).

The LS method for shape based reconstruction is well studied in electrical and electromagnetic imaging for simulated and experimental tank data (Santosa *et al* 1996; Litman *et al* 1998; Dorn *et al* 2000, Boverman *et al* 2003; Chan and Thai 2004; Soleimani *et al* 2006b; Soleimani 2007; Banasiak and Soleimani 2010); however, it has been never shown to be used for clinical data. This study, along with our previous work (Rahmati *et al* 2011) are the first implementation of the LSRM using time difference data for EIT clinical data. In this study, we use a difference formulation of LSRM to reconstruct a 2D image of the distribution of lung ventilation over an inflation manouevre (figure 4 and figure 5).

The remainder of the paper is organized as follows: in the next section, we formulate the image reconstruction algorithms using difference and absolute solvers for EIT (section 2.1). In subsection 2.2, we introduce into the LS technique employed for solving the inverse problem of EIT lung images. Subsection 2.3 discusses the details about the applied human data set, and the setting of the EIT system. In section 3, the experimental results are shown for the LSRM and the VBRM; and the performance of the difference mode LSRM for monitoring human lungs data is qualitatively and quantitatively compared with that of the VBRM. Section 4 presents discussions and conclusions.

## 2. Methods

### 2.1. Difference and absolute reconstruction methods

There are two primary reconstruction types in EIT: “absolute (static) imaging” which attempts to recover an estimate of the absolute conductivity of the medium from the achieved data frame, and “difference imaging” which attempts to recover an estimate of the change in conductivity between two times based on the change between two data frames,  $v_2$  and  $v_1$ . Difference EIT can compensate for measurement errors which do

not change between data frames. Difference EIT is based on a difference data vector,  $[y]_i = [v_2]_i - [v_1]_i$ , where  $i$  is the number of the measurements, or, to increase sensitivity to small measurements, the normalized difference data  $[y]_i = ([v_2]_i - [v_1]_i)/[v_1]_i$ . Using a finite element model (FEM), the medium is discretized into  $N$  elements with conductivity  $\sigma$ . The conductivity change vector  $x = \sigma_2 - \sigma_1$  is the change between the present conductivity distribution,  $\sigma_2$ , and that at the reference measurement,  $\sigma_1$ . The linearized difference forward solution for small changes in conductivities over time is given by (Adler *et al* 2007):

$$y = Jx + n, \quad (1)$$

where  $J$  is Jacobian or sensitivity matrix around the reference conductivity distribution, defined by  $\frac{\partial y}{\partial x}|_{\sigma_1}$  and  $n$  is the measurement noise, typically assumed to be an uncorrelated white Gaussian noise. In EIT, we need to solve an inverse problem to find an estimate of the conductivity, referred to as  $\hat{x}$ . The most common approach to find  $\hat{x}$  is the use of the Gauss-Newton (GN) algorithm for EIT reconstruction (Cheney *et al* (1990)). The GN method solves the EIT inverse problem by minimizing the the following quadratic residue (Adler *et al* 2007):

$$\|y - J\hat{x}\|_{\Sigma_n}^2 + \|\hat{x} - x_0\|_{\Sigma_x}^2, \quad (2)$$

where  $\Sigma_n^{-1}$  and  $\Sigma_x^{-1}$  are the covariance matrix of measurement noise and that of conductivity vector ( $\hat{x}$ ), respectively; and  $x_0$  represent the expected value of element conductivity changes. By solving (2) for  $\hat{x}$ , the linearized EIT inverse solution is obtained as (see Appendix A):

$$\hat{x} = (J^T J + R)^{-1}(J^T y + R x_0), \quad (3)$$

where  $R$  is the regularization matrix and  $x_0$  is the initial guess of the solution, which can be assigned to zero. In the remainder of this paper, the GN approach is considered the reference technique. GN image reconstruction typically results in smoothed images with blur edges, since the regularization matrix is based on a penalty filter for non-smooth images.

## 2.2. Level set method

One effective method to allow the reconstruction of sharp images is the LS method (Dorn *et al* 2000). The classic formulation of this method assumes that the reconstructed image can take only two conductivity values: one for background with value  $\sigma_b$  and another one for inclusions with value  $\sigma_i$ . The regions which form the background and the inclusions are defined by the LSF,  $\Psi$ : a signed distance function to identify the unknown interface between the two conductivities. The value of the LSF is zero on the interface, negative inside the interface, and positive outside.

Compared to the more typical VBRMs, the LSRMs allow more accurate reconstruction of the boundary shape of step changes of conductivity (high contrast objects). This is because most regularization schemes for the traditional methods, which

are necessary for stabilizing the inversion, have the side-effect of artificially smoothing the reconstructed images. Therefore, these schemes are not well-suited for reconstructing high contrast objects with sharp boundaries.

In order to arrive at a robust and efficient shape-based inversion method, there is a requirement to computationally model the moving shapes. The LS technique (Osher and Sethian, 1988; Sethian, 1999) is capable of modeling the topological changes of the boundaries. Figure 1 shows a two phases image reconstructed using the LSRM. The LSF  $\Psi$  has separated the zero LS surface into two regions: foreground (inclusions) and background. The mapping function  $\Phi$  projects the LSF to a 2D mesh to be applied for inverse solution calculation using FEM. Figure 1, right panel, shows the conductivity of the inclusions in black where the LSF is negative and that of background in white where the LSF is positive. To begin with, we need to define an initial LSF, which may be a circle on level zero; and then deform this initial LSF using a predefined energy functional iteratively. Figure 2 represents the steps as  $k$  represents the iteration number. After defining the initial LSF, the mapping function  $\Phi$  projects the LSF to a 2D mesh to be fed to difference solver block to calculate the system sensitivity matrix, Jacobian ( $J_k$ ), as well as differential potential vectors,  $\Delta d_i = [d_{real}]_i - [d(simulated)]_i$ . The next step is to update the energy functional via a Gauss-Newton formula,  $\Delta LSF_k$ . The initial LSF is then deformed by  $\Delta LSF_k$  generating a new LSF. This new LSF is fed again to difference solver block for another iteration if the current iteration number ( $k$ ) is not bigger than a maximum iteration number ( $K$ ). In the following, we discuss about the mathematical presentation of the LSRM.

In this technique, the shapes which define the boundaries, are represented by the zero LS of a LSF  $\Psi$ . If  $D$  is the inclusion with conductivity  $\sigma_i$  embedded in a background with conductivity  $\sigma_b$ , the boundary of the inclusion, which is also an interface between two materials, is given by the zero LS (Soleimani *et al* 2006b):

$$\partial D := \{r : \Psi(r) = 0\}, \quad (4)$$

where the image parameter at each point  $r$  is (Soleimani *et al* 2006b)

$$\sigma(r) = \begin{cases} \sigma_i & \text{for } \{r : \Psi(r) < 0\} \\ \sigma_b & \text{for } \{r : \Psi(r) > 0\} \end{cases}, \quad (5)$$

If we change this LSF for example by adding an update, we move the shapes accordingly. This update to a given LSF causes the shapes being deformed in a way which reduces an error residue (cost functional).

The LSRM combines the general idea of GN optimization approach with a shape-based inversion approach. To derive the LSRM, we define the mapping ( $\Phi$ ) which assigns a given LSF  $\Psi_D$  to the corresponding parameter distribution by  $\sigma = \Phi(\Psi_D)$ . The parameter distribution  $\sigma$  has the same meaning as in the traditional GN inversion scheme. The only difference is that in the shape-based situation it is considered as having only two values, namely an “inside” value and an “outside” value. In shape-based reconstruction approach, we are looking for the LSF  $\Psi_D$  which divides the image into two separate areas as foreground (inclusion) and background.

Having defined this mapping  $\Phi$ , we can now replace the iterated parameter  $\sigma_k$ , with the definition defined in (5), by  $\sigma_k = \Phi(\Psi_D) = \Phi(\Psi_k)$ . Instead of the forward mapping  $F(\sigma)$ , where function  $F$  maps the electrical conductivity distribution to the measured data, we need to consider now in the new GN type approach the combined mapping (Soleimani *et al* 2006b):

$$d(\Psi) = G(\Phi(\Psi)), \quad (6)$$

where  $d$  is data point matrix,  $G$  is system matrix, and  $\Phi(\Psi)$  stands for conductivity, see figure 1.

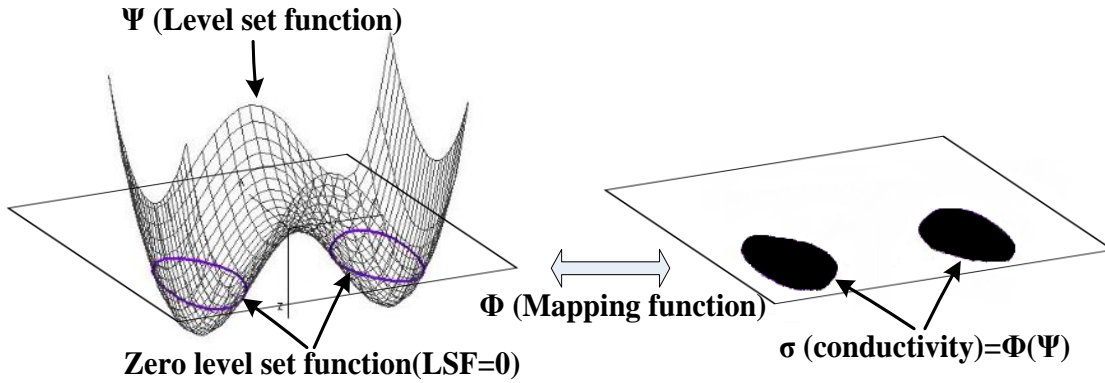


Figure 1: Level set function mapping to a 2D plane. From left to right columns, The 3D representation of an arbitrary level set function and its zero level set function crossing zero level set surface, and 2D mapping of the level set function on the zero level set surface.

According to the chain rule, the LS sensitivity matrix ( $J_{LS}$ ) can be written as below:

$$\begin{aligned} J_{LS} &= \frac{\partial d}{\partial \Psi} = \left( \frac{\partial G}{\partial \Phi(\Psi)} \right) \left( \frac{\partial \Phi(\Psi)}{\partial \Psi} \right) \\ &= (J_{GN})(M), \end{aligned} \quad (7)$$

where  $\frac{\partial G}{\partial \Phi(\Psi)}$  stands for the traditional GN sensitivity matrix ( $J_{GN}$ ), and we define  $\frac{\partial \Phi(\Psi)}{\partial \Psi} = M$ . Then, the new GN update (Soleimani *et al* 2006b) is as follows (see Appendix A) :

$$\begin{aligned} \Psi_{k+1} &= \Psi_k + \lambda \left[ (J_{(LS,k)}^T J_{(LS,k)} + \alpha^2 L^T L)^{-1} (J_{(LS,k)}^T (d_{real} - d(\Psi_k))) \right] \\ &\quad - \left[ \alpha^2 L^T L (\Psi_k - \Psi_{int}) \right] = \Psi_k + GN_{update} \\ &= LSF(k) + \Delta LSF, \end{aligned} \quad (8)$$

where  $\Psi_{int}$  in the update term corresponds to the initial estimate of the LSF. There are two parameters  $\lambda$  and  $\alpha$  to be tuned in this LS formulation. Figure 2 illustrates the algorithm to calculate the above update formula. The optimal choice of the two parameters,  $\lambda$  and  $\alpha$ , depends on the mesh density, the conductivity contrast and the initial guess (Soleimani *et al* 2006a). The length parameter  $\lambda$  and the  $\alpha$  both

affect the magnitude of the LSF displacement; however,  $\lambda$  makes the main effect on the displacement, changing the shape of inclusion, in a given update. The higher the  $\lambda$ , the higher the LSF displacement will be. The effect of the regularization parameter  $\alpha$  depends on the choice of the regularization operator  $L$ . An identity matrix for  $L$  increases the stability of the inversion by reduced smoothing of the LSF. However, a first order difference operator for  $L$  will smooth the LSF (Soleimani *et al* 2006a). As  $\alpha$  increases, the smoother the final LSF tends to be. A large value for  $\alpha$  prevents the reconstruction algorithm from being able to separate close objects (low distinguishability). In our experiments, the choice of  $L$  as the identity operator was made to improve distinguishability. In our results, we have put a value of zero for our initial guess of  $\Psi_{int}$  in the above shape-reconstruction form.

### 2.3. Experimental data

Experimental data were obtained in the study described by Pulletz *et al* (2011). Briefly, human breathing data were acquired from eight patients with healthy lungs (age:  $41 \pm 12$  years, height:  $177 \pm 8$  cm, weight:  $76 \pm 8$  kg, mean  $\pm$  std.) and eighteen patients (age:  $58 \pm 14$  years, height  $177 \pm 9$  cm, weight:  $80 \pm 11$  kg) with acute lung injury (ALI).

All patients were intubated and mechanically ventilated. The experimental procedure consisted of a low flow inflation pressure-volume manoeuvre applied by the respirator (Evita XL, Draeger, Luebeck, Germany), starting at an expiratory pressure of 0 cmH<sub>2</sub>O and ending when either a) the gas volume reached 2L, or b) the measured airway pressure reached 35 cmH<sub>2</sub>O. Airway gas flow, pressure and volume were recorded at a sampling rate of 126 Hz. An example pressure curve during the inflation protocol is shown in Figure 4. EIT data were acquired on sixteen self-adhesive electrodes (Blue Sensor L-00-S, Ambu, Ballerup, Denmark), placed at the 5th intercostal space in one transverse plane around the thorax, while a reference electrode was placed on the abdomen. EIT data were acquired at 25 frames per second, with an adjacent stimulation and measurement protocol, using current stimulation at 50 kHz and 5 mArms. Overall, 477 EIT data frames are acquired per inflation manoeuvre.

## 3. Experimental results

Images were reconstructed on a mesh roughly conforming to the anatomy of the subject, and the two different reconstruction algorithms (the VBRM and the LSRM) were tested on the clinical data (figure 3 - figure 6). Figure 3 shows the reconstructed images of ventilation in a lung healthy patient measured based on the difference signal between start and end inflation. As inspired air increases, the resistivity of the lungs increases which has been shown as blue regions in the reconstructed images in figure 3. The reconstructed images clarify the difference between LSRM and VBRM in terms of creating sharper reconstructions with larger contrasts at the interface between

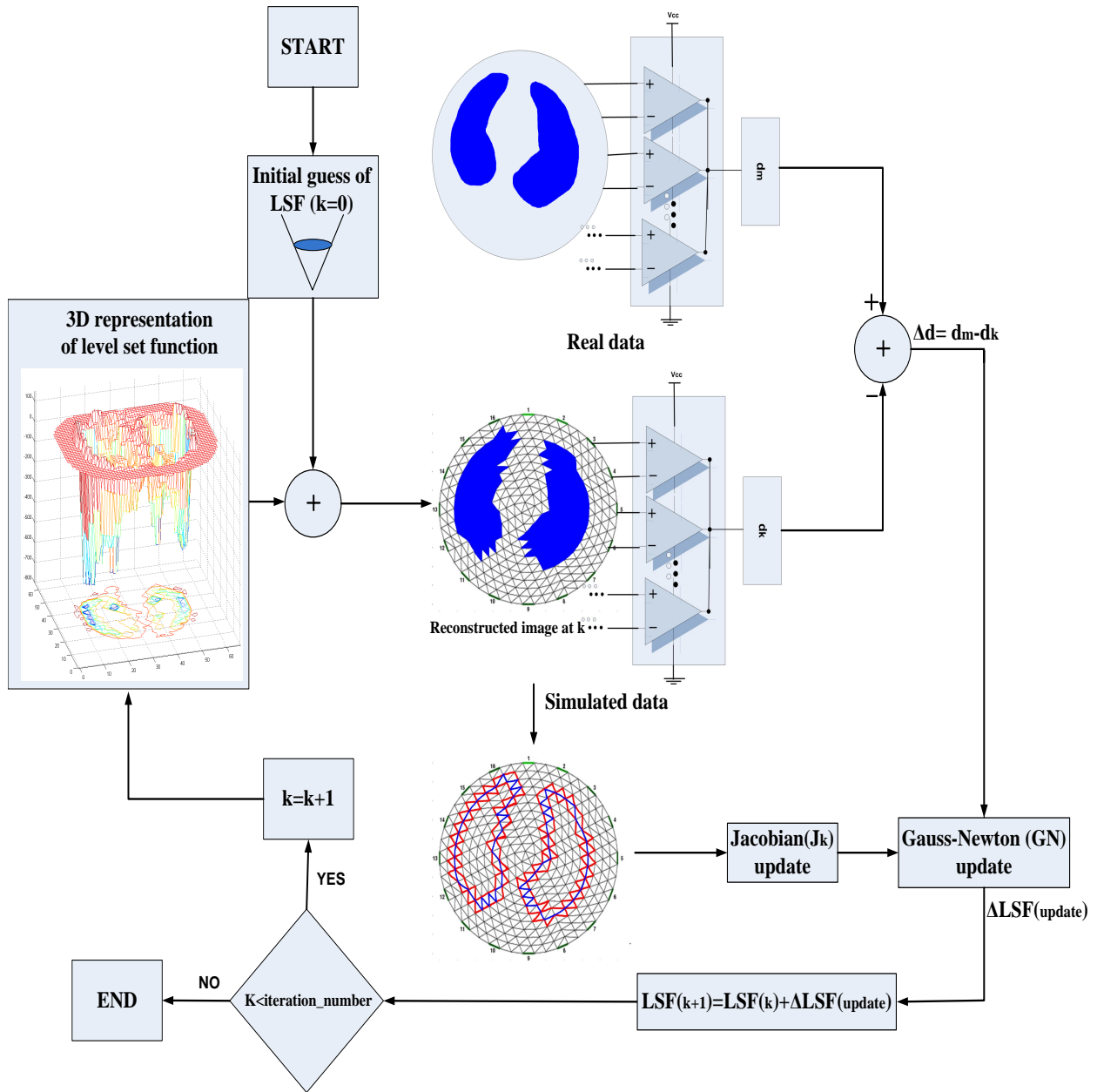


Figure 2: The level set based reconstruction algorithm using difference solver. The level set based reconstruction method comprises the following steps, respectively: level set function initial guess, inverse difference solver, Gauss-Newton update, level set function displacement by the given update, and iteration number increment.

the inclusion and the background, presenting step change of conductivity. The final reconstructed image by the LSRM represents the air distribution inside the lungs after 30 iterations (figure 3(c)).

Figure 4 shows the LSRM reconstruction images for a patient with healthy lungs over the inflation manoeuvre measured for three different times from start of the inflation manoeuvre: 5.17s, 10.34s, and 17.24s. The measurement times are selected to show an

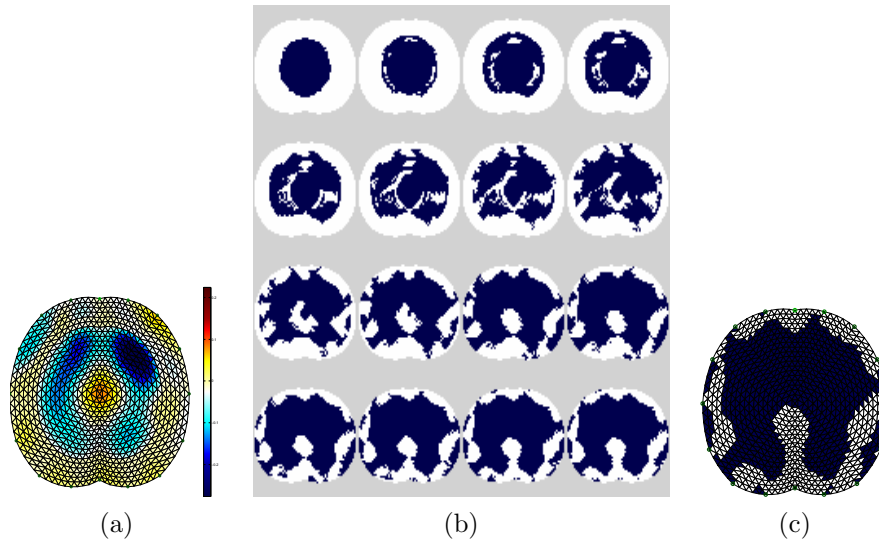


Figure 3: The qualitative comparison between the level set based reconstruction method and the voxel based reconstruction method in difference mode at the maximum airway pressure of the inflation manoeuvre for a patient with healthy lungs . (a) The lung reconstructed image using the voxel based reconstruction method. (b) The first sixteen iterations of the level set based reconstruction method for the same data as (a). (c) The final human lungs reconstructed image using the level set based reconstruction method at iteration 30.

initial airway pressure, a middle airway pressure, and a high airway pressure. The reconstruction algorithms for the LSRM and the VBRM used a finite element mesh (1600 elements). For all images of the VBRM for the patients (figure 3 - figure 5), the colour axis (color map) was scaled to the same maximum value to maximize the displayed contrast. The LSRM results when comparing with the VBRM ones show more details about the shape of the air distribution inside the lungs. The shape of the air distribution of the VBRM images for different frames is very similar to each other (circular shapes). However, the LSRM images clearly show the difference in the shape of the air distribution for different time frames.

Figure 5 shows the LSRM reconstruction images for an ALI patient along the inflation manoeuvre measured for the same measurement times as figure 4. The density of the meshes are the same as in figure 4 (1600 elements). The VBRM offers less changes in the shape of the air distribution inside the lungs for the ALI patient, the second row of Figure 5. However, the LSRM better show the changes of the air distribution for different frames, the third row of Figure 5.

For the VBRM, a region of interest (ROI), describing the lungs, was identified as 25% of the maximum conductivity change (Pulletz *et al* , 2011). For the LSRM, the ROI is the region with negative LSF, where there exists the inclusion. The VBRM and the LSRM were compared by calculating the normalized summation of elements

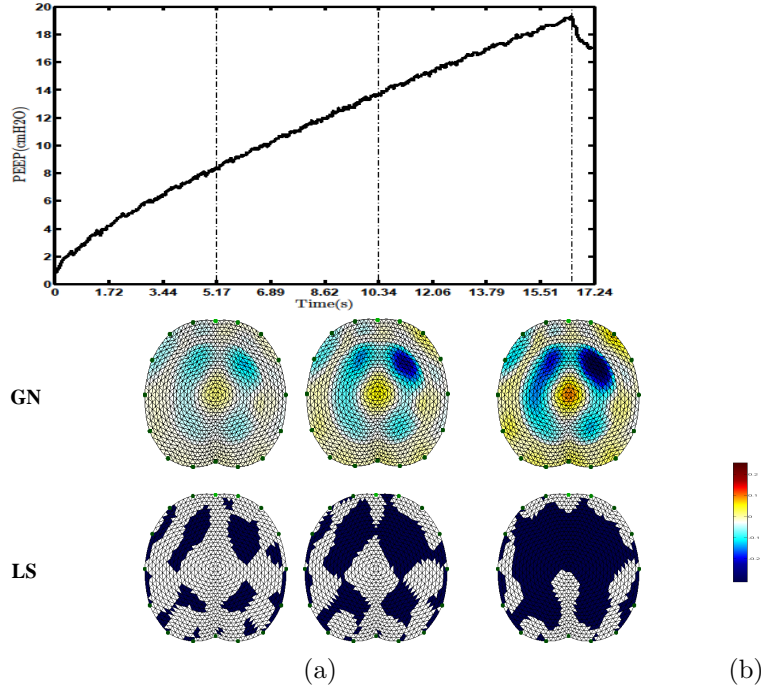


Figure 4: The clinical results of the level set based reconstruction method over the inflation manoeuvre of a patient with healthy lungs. (a) The first row represents the inflation manoeuvre of the patient with healthy lungs, the second row is the results from the voxel based reconstruction method, and the third row is the clinical results of the level set based reconstruction method for the same patient. (b) The color map of the voxel based reconstruction method. The reconstructed images in (a) are shown for three different measurement times: 5.17s (an initial airway pressure) , 10.34s (a middle airway pressure), and 17.24s (a high airway pressure).

conductivities (NSEC) over the ROI as follows:

$$NSEC(j) = \frac{\sum_{i=1}^P \sigma_{ij}}{\sum_{i=1}^Q \sigma_{ij_{max}}} \quad (9)$$

where  $j$  is the frame at which the NSEC is calculated,  $P$  is the number of the elements inside the ROI for the frame  $j$ ,  $j_{max}$  is the frame at which the maximum lung inflation happens (maximum lung volume), and  $Q$  is the number of the elements inside the ROI for the frame  $j_{max}$ . The NSEC was calculated at seven evenly spaced time points along the inflation manoeuvre. Results were presented for lung healthy (figure 6(a)) and ALI (figure 6(b)) patients. For both algorithms, the NSEC increases with pressure as the lung volume increases. Our results show the NSEC curve is more non-linear for both algorithms for the ALI than lung healthy patients, which is consistent with the higher opening pressure of dependent lung regions in ALI patients.

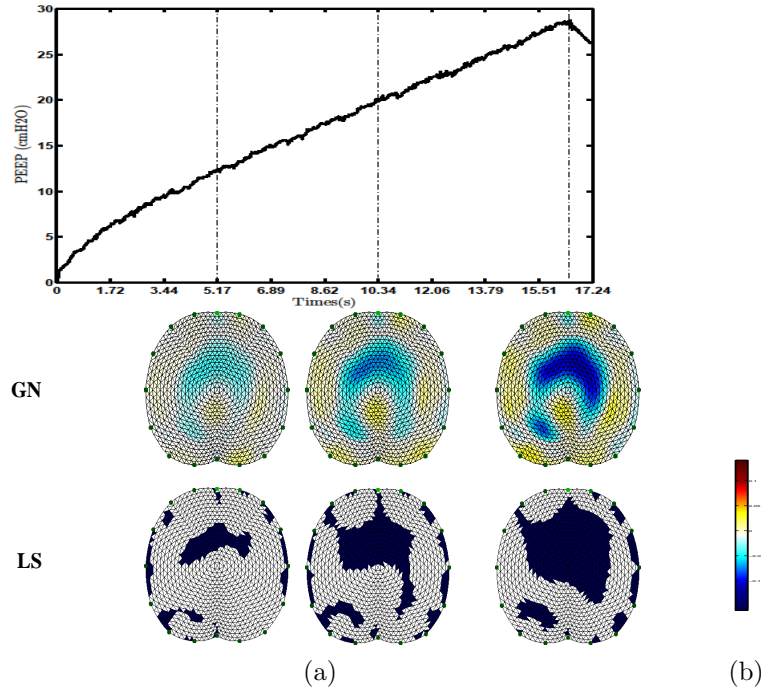


Figure 5: The clinical results of the level set based reconstruction method over the inflation manouevre of a patient with a heterogeneous lung disease. (a) The first row represents the inflation manouevre, the second row shows the voxel based reconstruction method results, and the third row is the clinical results of the level set based reconstruction method for the same patient. (b) The color map of the voxel based reconstruction method. The reconstructed images in (a) are shown for three different measurement times: 5.17s (an initial airway pressure) , 10.34s (a middle airway pressure), and 17.24s (a high airway pressure).

#### 4. Discussion and conclusion

We proposed the LSRM in difference mode for clinical EIT data of patient ventilation over the inflation manouevre. We report the first clinical results of applying the LSRM to monitor the air distribution inside the lungs using EIT. In the proposed difference mode LSRM, the inverse solution of Gauss-Newton formula updates the sensitivity matrix and consequently the LSF with every iteration. In the first iteration, the  $\Psi$  is chosen as initial guess. The initial guess is an arbitrary function, for example the definition of a circle. The updated LSF converges to a conductivity map that minimizes the error between measured and simulated data. The minimization of the error function finally leads to the division of the medium into two regions: the background and the foreground. The difference imaging LSRM depicts the capability of finding the big conductivity changes at the interface between lung and the background (figure 3). We follow a narrowband level set method, such as the value of the level set function is thresholded and it is zero at the interface between two materials. The advantage of the narrowband method is that it allows the shape evolution without the need to re-formulate the geometrial boundaries

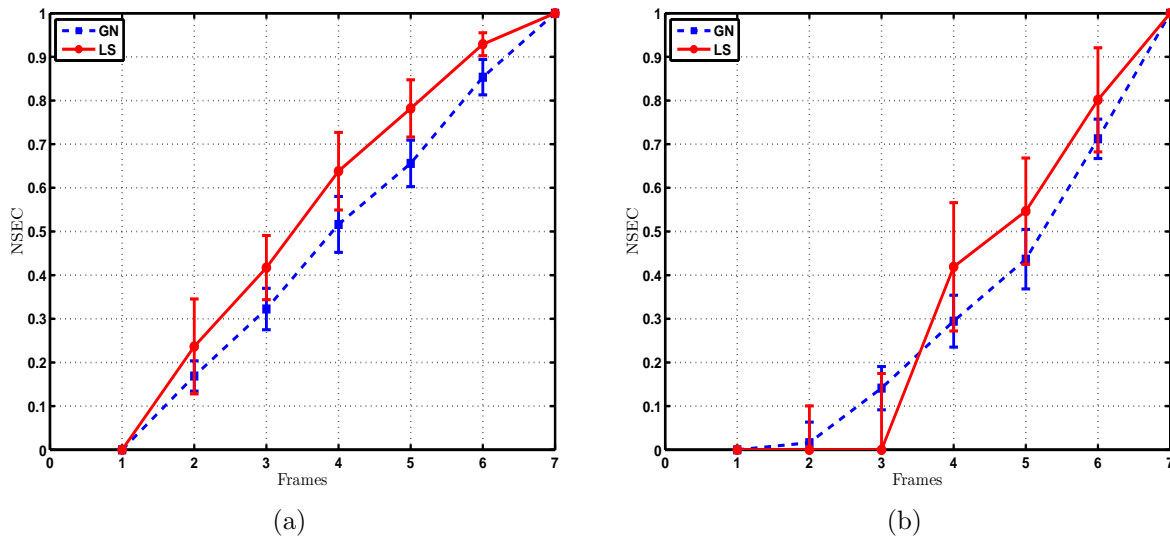


Figure 6: Normalized sum of element conductivities as a function of fraction of the inflation manoeuvre: (a) lung-healthy patients (b) Acute lung injury patients. In each case, the solid lines show example patients, while the distributions show the standard deviation over all patients in that class.

of the inclusions. The mapping function is used to discourage the reconstruction of the disconnected contours located at different levels. The update sensitivity matrix has been calculated on a narrow band region, involving the elements sharing an edge with the interface between foreground and background (see figure 2). The narrow band region makes the LSRM run faster when comparing with the LSRM calculating the sensitivity matrix over the whole elements for every iteration.

To achieve more accurate interface where there are more than two highly different conductivities inside the medium, such as lungs, heart, and the peripheral tissues, it is suggested to apply two different LSFs in defining the medium in the equation 2 (Dorn and Lesselier 2006; DeCezaro *et al* 2009).

Our results represent that the difference formulation of LSRM is suitable to be applied for clinical EIT data of patient ventilation over lung inflation (figure 3, figure 4, figure 5). Comparing with the VBRM, the LSRM shows high contrast lung images corresponding to the physiologically known shape of lung air distribution in these patients (figure 4, third row, and figure 5, third row). The NSEC curves (figure 6) are similar in shape in the LSRM to the VBRM, but show a slower start at the low lung inflation, reflecting perhaps some non-linearity for small conductivity changes.

In summary, we show that level set based image reconstruction techniques can be applied to clinical EIT data to produce plausible images. The results suggest that such level set approaches help to address the blurring of edges inherent in regularized algorithms. The proposed LSRM show promising results to help spur interest in using novel edge-preserving algorithms to practical EIT applications.

## 5. Appendix A

In this appendix, we show how to derive equation (3) from (2). Then, we explain how to minimize the error function, defined in (2), for the non linear case, such as the LSRM. The inverse solution of (2) can be calculated by minimizing the following error function:

$$e = \|y - F(x)\|^2 + \|x - x_0\|^2, \quad (10)$$

To minimize the error function, we take the first derivative of the error function with respect to  $x$ :

$$\begin{aligned} \frac{de}{dx} &= \frac{d}{dx} [(y - F(x))^t (y - F(x)) + (x - x_0)^t R (x - x_0)] = 0, \\ &= \frac{d}{dx} [y^t y - 2F(x)^t F(x) + (x - x_0)^t R (x - x_0)] = 0, \end{aligned} \quad (11)$$

We define  $J = \frac{dF}{dx}$ , thus we have:

$$\begin{aligned} \frac{de}{dx} &= -2J^t(x)y + 2J^t(x)F(x) + 2R(x - x_0) = 0, \\ J^t(x)F(x) + R(x - x_0) &= J^t(x)y, \end{aligned} \quad (12)$$

In linear case, we can define  $F(x) = Jx$ , and  $J(x) = J$ . Thus, we can write:

$$\begin{aligned} J^t Jx + R(x - x_0) &= J^t y, \\ (J^t J + R)x &= J^t y + Rx_0, \\ x &= (J^t J + R)^{-1} (J^t y + Rx_0), \end{aligned} \quad (13)$$

where the last equation is in agreement with (3).

The following shows the minimization of the error function to derive (8). For the non-linear case, if we use  $F(x)$ , starting at estimate  $x_k$ , then:

$$F(x) = J(x_k)(x - x_k) + F(x_k), \quad (14)$$

Applying the notation changes of  $F(x_k) = F_k$ , and  $J(x_k) = J_k$ , we can write:

$$\begin{aligned} J^t(x)F(x) + R(x - x_0) &= J^t(x)y, \\ J_k^t(J_k(x - x_k) + F_k) + R(x - x_0) &= J_k^t y, \\ J_k^t J_k(x - x_k) + R(x - x_0) &= J_k^t (y - F_k), \\ (J_k^t J_k + R)(x - x_k) &= J_k^t (y - F_k) - R(x_0 - x_k), \\ x - x_k &= (J_k^t J_k + R)^{-1} (J_k^t (y - F_k) - R(x_0 - x_k)), \end{aligned} \quad (15)$$

The solution  $(x)$  to (15) is described as  $x_{k+1}$ . Therefore, we can define  $\Delta_{k+1} = x_{k+1} - x_k$ . In the LSRM, the evolution function is as follows:

$$\Phi(\Psi_{k+1}) = \Phi(\Psi_k) + \lambda(\Delta\Phi(\Psi)), \quad (16)$$

where  $\Phi(\Psi) = x$ ; and  $\Delta\Phi(\Psi) = \Delta x$ ,

The error function is defined as follows:

$$\Delta\Phi(\Psi) = \|y - F(x)\|^2 + \|x - x_0\|^2, \quad (17)$$

The jacobean ( $B$ ) is defined as below:

$$\begin{aligned} B &= JM, \\ B^t &= M^t J^t; B^t B = M^t J^t JM, \end{aligned} \tag{18}$$

Minimizing the error function results in (8):

$$\begin{aligned} \Psi_{k+1} &= \Psi_k + \lambda \left[ (J_{(LS,k)}^T J_{(LS,k)} + \alpha^2 L^T L)^{-1} (J_{(LS,k)}^T (d_{real} - d(\Psi_k))) \right] \\ &\quad - \left[ \alpha^2 L^T L (\Psi_k - \Psi_{int}) \right] = \Psi_k + GN_{update} \\ &= LSF(k) + \Delta LSF, \end{aligned} \tag{19}$$

where  $R = \alpha^2 L^T L$ .

## References

- Adler A, Arnold J H, Bayford R, Borsic A, Brown B, Dixon P, Faes T J C, Frerichs I, Gagnon H, Grber Y, Grychtol B, Hahn G, Lionheart W R B, Malik A, Patterson R P, Stocks J, Tizzard A, Weiler N, Wolf G K 2009 *GREIT: a unified approach to 2D linear EIT reconstruction of lung images Physiol. Meas. Journal* vol 30 p 35
- Adler A, Dai T and Lionheart W R B 2007 *Temporal Image Reconstruction in Electrical Impedance Tomography Physiol. Meas.*, vol 28 p 1
- Boverman G, Khames M and Miller E L 2003 *Recent work in shape-based methods for diffusive inverse problems Review of Scientific Instruments* p 2580
- Banasiak R and Soleimani M 2010 *Shape based reconstruction of experimental data in 3D electrical capacitance tomography NDT&E International* vol 43 p 241
- Chan T F and Tai X C 2004 *Level set and total variation regularization for elliptic inverse problems with discontinuous coefficients Journal of Computational Physics* p 40
- Cheney M, Isaacson D, Newell J C, Simske S and Goble J C 1990 *NOSER: an algorithm for solving the inverse conductivity problem Int. J. Imaging Syst. Technol.* vol 2 pp 66
- Church P, McFee J E, Gagnon S and Wort P 2006 *Electrical impedance tomographic imaging of buried landmines IEEE Transaction of Geoscience and Remote Sensing* vol 44 p 2407
- DeCezaro A, Leito A, Tai X C 2009 *On multiple level-set regularization methods for inverse problems Inverse Problem* vol 25
- Dorn O, Miller E L and Rappaport C M 2000 *A shape reconstruction method for electromagnetic tomography using adjoint fields and level sets Inverse Prob.* vol 16 p 1119
- Dorn O, Lesselier D 2009 *Level set methods for inverse scatteringsome recent developments Inverse Problem* vol 25 p 11
- Frerichs I, Pulletz S, Elke G, Zick G, Weiler N 2010 *Electrical Impedance Tomography in Acute Respiratory Distress Syndrome The Open Nuclear Medicine Journal* vol 2 p 110
- Frerichs I, Dudykevych T, Hinz J, Bodenstein M, Hahn G, Hellige G 2001 *Gravity effects on regional lung ventilation determined by functional EIT during parabolic flights Journal of Applied Physiology* vol 91 p 39
- Frerichs I 2000 *Electrical impedance tomography (EIT) in applications related to lung and ventilation: a review of experimental and clinical activities Physiological Measurement Journal* vol 21 p 1
- Gao N, Zhu S A, He B 2006 *A New Magnetic Resonance Electrical Impedance Tomography (MREIT) Algorithm: RSM-MREIT Algorithm with Applications to Estimation of Human Head Conductivity Physics in Medicine and Biology* vol 51 p 3067
- Hahn G, Beer M, Frerichs I, Dudykevych T, Schroder T, Hellige G 2000 *A simple method to check the dynamic performance of electrical impedance tomography systems. Physiol Meas* vol 21 p 53-60
- Litman A, Lesselier D and Santosa F 1998 *Reconstruction of a two-dimensional binary obstacle by controlled evolution of a level-set Inverse Prob.* vol 14 p 685

- Loke M H, and Barker R D 1996a *Rapid least-squares inversion of apparent resistivity pseudo-sections using quasi-Newton method Geophysical Prospecting* vol 48 p 181
- Loke M H, Barker R D 1996b *Practical techniques for 3D resistivity surveys and data inversion Geophysical prospecting* vol 44 p 499
- Manwaring P, Halter R, Wan Y, Borsic A, Hartov A, Paulsen K 2008 *Arbitrary geometry patient interfaces for breast cancer detection and monitoring with electrical impedance tomography Conf Proc IEEE Eng Med Biol Soc.* p 1178
- Osher S and Sethian J 1988 *Fronts propagation with curvature dependent speed: Algorithms based on hamilton-jacobi formulations J. Computational Phys.* vol 56 p 12
- Osher S and Paragios N 2003 *Level Set Methods in Geometric Level Set Methods in Imaging, Vision, and Graphics* (Eds. New York, NY: Springer) p 1
- Polydorides N, Lionheart W R B and McCann H 2002 *Krylov subspace iterative techniques: On the detection of brain activity with EIT IEEE Trans. Med. Imag.* vol 21 no 6 p 596
- Pulletz S, Adler A, Kott M, Elke G, Gawelczyk B, Schdler D, Zick G, Weiler N, Frerichs I 2011 *Regional lung opening and closing pressures in patients with acute lung injury Journal of Critical Care* in press.
- Rahmati P, Soleimani M, Adler A 2011 *Level Set Based Reconstruction Algorithm for EIT Lung Images The 12th International Conference in Electrical Impedance Tomography (EIT 2011)*
- Santosa V 1996 *A level-set approach for inverse problems involving obstacles in ESAIM: Control, Optimization and Calculus of Variations*1 p 17
- Sethian J A 1999 *Level Set Methods and Fast Marching Methods* (2nd ed. Cambridge, U.K.: Cambridge Univ. Press)
- Soleimani M, Dorn O and Lionheart W R B 2006a *A Narrow-Band Level Set Method Applied to EIT in Brain for Cryosurgery Monitoring IEEE Trans. Bio. Eng.* vol 53 No 11
- Soleimani M, Lionheart W R B and Dorn O 2006b *Level set reconstruction of conductivity and permittivity from boundary electrical measurements using experimental data Inverse Problems in Science and Engineering* vol 14 No 2 p 193
- Soleimani M 2006c *Electrical impedance tomography imaging using a priori ultrasound data Biomedical Engineering Online* vol 5
- Soleimani M 2007 *Level-Set Method Applied to Magnetic Induction Tomography using Experimental Data Research in Nondestructive Evaluation* vol 18 p 1